Estimating dose and interaction of X-rays with cellulose-based fibrous materials using micro-computed tomography

ANDREAS APFOLTER, PETRA SCHINDLER, VIKTORIA HABERL, MAXIMILIAN FUCHS, KARIN ZOJER, EDUARDO MACHADO CHARRY, AND ROBERT SCHENNACH

ABSTRACT: Micro-computed tomography (μCT) has a reputation as a nondestructive analysis method. Unfortunately, this leads to the common misconception that radiation damage of the sample does not play a role. With the increased use of μCT in laboratory-based machines, more and more cellulose-based materials are studied. In this paper, we show with three examples that radiation damage is important in dry and wet paper and in viscose fibers.

In an attempt to quantify radiation damage, we came up with a workflow that enables researchers to predict the X-ray dose within a laboratory-based μCT machine. This gives researchers the possibility to quantitatively judge the influence of radiation damage on each measured sample. While one cannot extend the measured doses from one machine to another, one can still apply the work flow presented in this study to any μCT setup. In this way, it is possible to minimize radiation damage by choosing the best parameters in a μCT for obtaining perfect data with no or little radiation damage.

Application: Radiation damage occurs quite often in μCT measurements. In this work we show how the X-ray dose can be estimated and then used to optimize the μCT parameters to get both, high quality data and little-or-no radiation damage.

When Wilhelm Roentgen discovered X-rays, he, like other researchers, did not realize that X-rays could cause damage to living organisms. It was not until the scientific community realized that X-rays are ionizing radiation that they began to understand their effects on biological systems. Today, X-rays are used safely in clinical and non-clinical settings. Unfortunately, this has led many people to ignore potential radiation damage when working with X-rays in analytical tools such as X-ray diffraction (XRD) and micro-computed tomography (μCT). In the case of medical CT, machines are built to minimize the radiation dose to the patient. In materials science, only non-living samples are studied, leading to a general ignorance of radiation damage to the measured samples.

When the first μCT measurements on nonwoven papermaker felt samples were done by Bloch and Thibauld [1], people concentrated on the new insights into the porous structure. With the advent of more powerful laboratory devices in recent years, more and more cellulose-based materials are being studied [2-8].

The extent of radiation damage within a medium depends on the locally deposited energy, the absorbed dose, D_{med}. Knowing the dose the sample has absorbed is therefore crucial for detecting, interpreting, and possibly preventing radiation damage. In this publication, we first propose how to determine the absorbed dose in a laboratory-based μCT system; in our case a Tescan Unitom XL, known as XL in this paper, with a reflection source and a Tescan Unitom HR, known here as HR, with a transmission source (Tescan; Brno, Czech Republic). The described method can be extended to any μCT system, including synchrotron-based μCT setups. Second, we will use spectroscopy-based methods to investigate radiation-induced changes in cellulosic materials under dry conditions. Third, we showcase macroscopically visible alterations from slight changes in color via changes in mechanical properties (brittleness of the radiated sample) to bubble formation in paper samples immersed in water. Our aim is to find optimal parameters to reduce the damage to the sample due to its interaction with X-rays and optimal parameters for the μCT measurement.

METHODS AND MATERIALS

Prediction of the dose received by the sample

The quantity of interest is the sum of all energy deposited in the medium, i.e., the absorbed dose D_{med}. Therefore, the final goal is to predict the dose that a sample of a given material and size will receive during a given exposure time at a given distance from the X-ray source, depending on the operating parameters of the X-ray source. The overview in **Fig. 1** guides our description of the proposed sequence of measurements and intermediate quantities needed to estimate a dose solely knowing the operation parameters, exposure time, sample position, material, and extension.

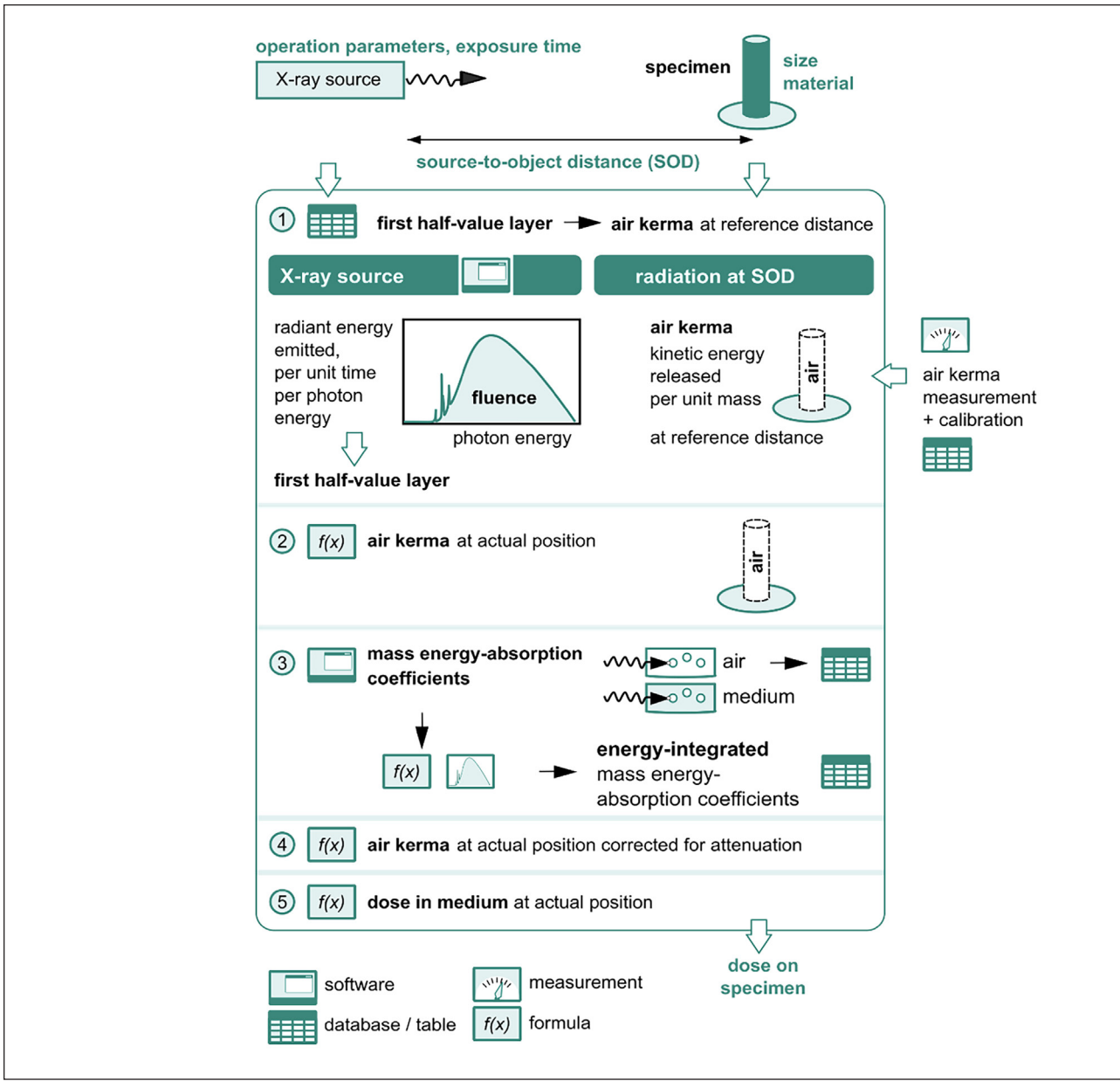

1. Schematic workflow to estimate the dose a sample/specimen receives during a micro-computed tomography (µCT) scan in five steps. The dose is determined for a given X-ray source, its operation parameters, the exposure time, distance of the sample to the X-ray source, and size and material of sample. Symbols indicate whether the individual steps require additional information from databases or software, produce look-up tables, or the use of a formula. Before step (1) can be realized, measurements specific for the X-ray device are necessary.

The key idea is to infer D_{med} from the kinetic energy released per unit mass, K_{med} (kerma), that quantifies the energy initially transferred from the radiation to the photon-produced electrons in a volume of a medium exposed to the X-ray beam. For photon energies $E < 300$ keV, in combination with charged particle equilibrium, the value of K_{med} corresponds in sufficiently accurate approximation to D_{med}; i.e., it is sufficient to reliably establish the order of magnitude (see Appendix for underlying rationale) [9,10]. Note that D_{med} and kerma K, despite being different quantities, share the same unit J/kg, known as gray (Gy).

The K_{med}, in turn, can be directly obtained from the value of air kerma free-in-air, K_{air}, because the ratio K_{med}/K_{air} is given by the ratio of mass energy-absorption coefficients integrated over the range of photon energies emitted from the X-ray source between the medium and air (compare with [10] and Appendix).

The first step (Fig. 1) relates the intensity output and energy spectra of the X-ray source for different operation parameters to the expected K_{air} for air at a reference distance within the setup.

Quantifying intensity output of different X-ray sources with their operation modes

Parameters such as tube potential U, target current I, and used filters influence the number and energy of emitted X-ray photons and, hence the fluence spectrum (i.e., radiant energy emitted, per unit time per photon energy). This spectrum is needed later to obtain the integrated mass energy absorbance coefficients.

The first half-value layer, HVL_1, serves as a beam quality index and is considered sufficient to characterize and distinguish X-ray beams. The HVL_1 refers to the thickness of an absorber, typically high-purity aluminum (Al) or copper (Cu), which reduces the air kerma to 50% of its initial value.

Based on the main parameters of the two examined X-ray devices (listed in **Table A-I** in the Appendix), the range of HVL_1, associated fluence spectra, and K_{air} values were calculated with SpekPy, a free software toolkit for calculating and manipulating the fluence spectra of X-ray tubes [11,12]. Such calculated K_{air} values can be used for operation modes, for which no K_{air} measurement was done. In the case of the transmission type tube XWT-160-TCNF (X-RAY Worx; Garbsen, Germany), the calculations were done in combination with aRTist [13], a software capable of calculating spectra for transmission anodes. A total of 224 fluence spectra were calculated and analysed for tube potentials from 20 kV to 180 kV, at 10 kV intervals, at 400 mm source-to-object distance (SOD) for both X-ray tubes and all additional filters. Appendix **Fig. A-1** shows examples of the calculated fluence spectra Φ_{norm} normalized to the total fluence for the XWT-160-TCNF tube for tube potentials of 40 kV, 80 kV, 100 kV, and 160 kV combined with a selection of filters. The determined HVL_1 range from 0.09 mm Al up to 16.6 mm Al.

Obtaining air kerma values for the X-ray sources

Measuring K_{air} for a wide range of combinations of tube potentials U and filtrations requires two chamber types that complement each other. Intensity output measurements were performed with a PTW 30013 (0.6 cm^3) cylindrical ionization chamber and a PTW 23342 (0.02 cm^3) plane-parallel ionization chamber (PTW; Freiberg, Germany). Due to its small energy dependence, the PTW 30013 is the chamber of choice for filtered photon beams with tube potentials above 50 kV [14]. However, low energy photons in lightly filtered photon beams are absorbed by the chamber wall, and the chamber response decreases rapidly. Due to the thin entrance window, the PTW 23342 is best suited for the measurement of low energy photons.

The K_{air} values were measured at the reference (SOD) of 400 mm for a wide range of HVL_1 representing the variation of the tube potentials U and the additional filters used. The readings from both ionization chambers were corrected for changes in air density inside the chamber volume relative to the calibration conditions caused by air pressure and temperature variations.

Ionization chambers measure the charge created in the chamber by the high-energy photons of the beam. The amount of charge produced is proportional to the beam intensity and exhibits a dependency on the photon energy. Therefore, the chamber reading $K_{air,\,read}$ must be corrected with an energy dependent calibration factor, N_K, to get the actual K_{air}via $K_{air} = N_K\, K_{air,\,read}$.

The required calibration factors are determined based on standard calibration factors. First, a series of chamber calibration factors N_K for a set of standard beam qualities supplemented with off-label calibrations for a wide range of beam qualities were obtained from a secondary standards dosimetry laboratory, as shown in **Table A-III** and as dots in **Fig. A-2** (both in the Appendix). Second, interpolating these N_K values to the HVL_1 values related to our tubes (calculated by aRTist and SpekPy, see Appendix Fig. A-1) provide the calibration factors needed to quantify K_{air} (Fig. A-2).

The calibration factors N_K indicate the HVL_1 range in which the measured K_{air} values can be trusted. The PTW 30013 should not be used for measurements $HVL_1 < 2$ mm Al (indicated by a steep increase in N_K, Fig. A-2), while the PTW 23342 is not suitable for measurements in the range $HVL_1 > 4$ mm Al. In contrast, N_K of PTW 30013 being practically constant 0.89 for $HVL_1 > 2$ mm Al encourages an extrapolation of the calibration factors up to 16 mm Al to cover the HVL_1 range needed.

The measured K_{air} values, normalized to a current-time product of 1 mAs, at SOD = 400 mm for the two X-ray devices are shown for different tube potentials and filters in **Fig. 2**. The list of K_{air} values is compiled for HR XWT 160 TCNF in Table A-III and for XL XWT 190 CT in **Table A-IV** in the Appendix, respectively. Measurements in fields with low HVL_1 were done with PTW 23342, and measurements with high HVL_1 were done with PTW 30013. Note that the results for tube HR XWT 160 TCNF combined with a tin (Sn) filter rely solely on aRTist and SpekPy calculations, as no measurements were done in this case.

Air kerma values for varying SODs

Neglecting beam attenuation in air in front of the sample and the radiation scattered into the sample position, e.g., due to scattering from the walls, the kerma K increases with decreasing SOD according to an inverse square law:

$$\frac{K_{air,SOD}}{K_{air,400\,mm}} \approx \left(\frac{400\,mm}{SOD}\right)^2 \qquad (1)$$

In a synchrotron environment, the distance correction must be formulated differently, as there the X-ray beam does not diverge.

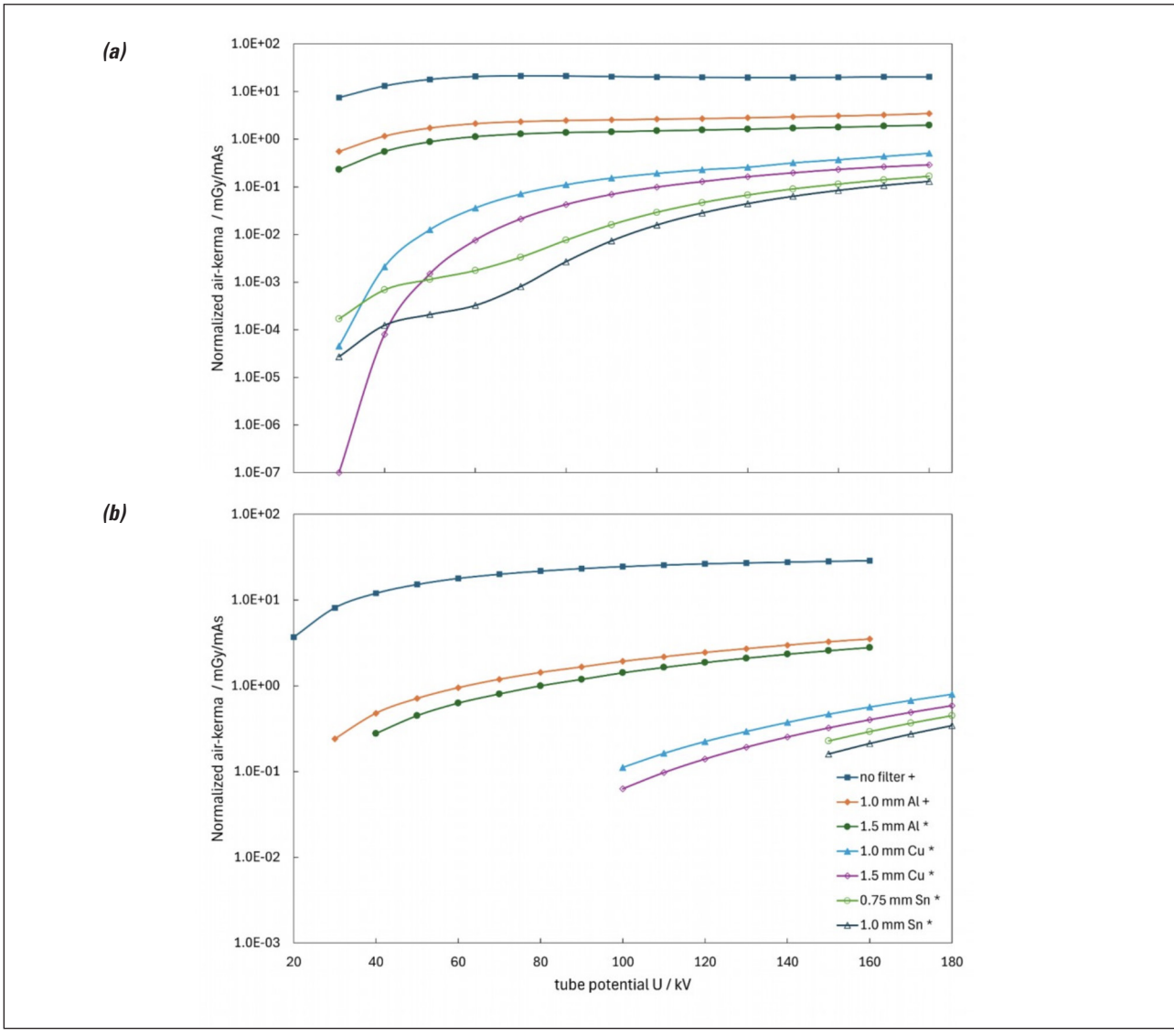

2. Air kerma free-in-air K_{air} normalized to a current-time product of 1 mAs as a function of tube potential U and applied filter for (a) tube 1 (HR XWT 160 TCNF) and (b) tube 2 (XL XWT 190 CT) at SOD = 400 mm. To obtain the air kerma for an actual scan, the air kerma per current-time product must be multiplied by the tube current and the scan time. Note that (a) and (b) have the same x-axis. The + means measured with PTW 23342; the * means measured with PTW 30013; and the # means calculated with aRTist/SpekPy [11-13] (no measurements were taken).

Inferring the kerma in the medium from air kerma

For a given photon energy E, the kerma in the medium, K_{med}, is related to K_{air} via the ratio of the mass energy-absorption coefficients μ_{en}/ρ in the medium and air, respectively (refer to the Appendix for details):

$$K_{med} \approx K_{air} \times \frac{\left[\frac{\mu_{en}(E)}{\rho}\right]_{med}}{\left[\frac{\mu_{en}(E)}{\rho}\right]_{air}} \quad (2)$$

In case of a photon beam with a photon fluence spectrum Φ_{med}, the mass energy-absorption coefficients must be integrated over the range of photon energies:

$$K_{med} \approx K_{air} \times \frac{\int_0^{E_{max}} E \times \Phi_E \times \left[\frac{\mu_{en}(E)}{\rho}\right]_{med} dE}{\int_0^{E_{max}} E \times \Phi_E \times \left[\frac{\mu_{en}(E)}{\rho}\right]_{air} dE} \quad (3)$$

Sources for finding the mass energy-absorption coefficients for a wide range of materials and energies are given in Section A.3 of the Appendix.

Considering beam attenuation prior to reaching sample position of interest

For extended samples, the attenuation of the primary fluence and the additional fluence due to increased scatter must be accounted for. Particularly for low energy photon beams (no filter), the attenuation of even thin materials in

front of the sample (e.g., sample in a small tube of water) cannot be neglected. The effect of the attenuating material thickness x can approximately be accounted for by using the mass attenuation coefficient μ/ρ and applying the exponential attenuation law:

$$K_{air}(x) = K_{air} e^{-\frac{\mu}{\rho}\rho x} \quad (4)$$

Mass attenuation coefficients μ/ρ for monoenergetic photons can easily be obtained from the XCOM Photon Cross Section Database [15]. In case of non-monoenergetic photon spectra, the attenuation can be calculated by using SpekPy [11,12]. Then, $K_{air}(x)$ replaces K_{air} in Eq. 2 and Eq. 3.

Estimating the dose

Based on a series of assumptions on the main contribution to the energy deposited in the sample (compiled in the Appendix), it is possible to approximate the dose D_{med} with the value of K_{med}:

$$D_{med} \approx K_{med} \quad . \quad (5)$$

One has to bear in mind that the dose values are only true for the two µCT setups used here. The same is true for the calibration factors used in the experiments.

Radiation damage on dry and wet cellulosic materials

To illustrate the effects of radiation on cellulosic materials under different conditions, we designate a set of papers and viscous fibers for detailed analysis.

Materials

Paper (P) comprises fresh softwood fibers with a basis weight of 100 g/m². This paper lacks any intentional fillers and did not undergo any mechanical post-treatment. Due to hard sizing with alkenyl succinic anhydride (ASA), the contact angle with water is 122° [16]. The three selected inkjet papers, I1, I2, and I3, primarily differ in their degree of sizing. These uncoated papers are made from hardwood fibers with precipitated calcium carbonate (PCC) as filler. More details on the papers can be found in **Table A-V** in the Appendix. In addition, samples of commercial cotton wool of viscous fibers (V), in the form of loose fibers and a tampon were used.

Paper (P) and viscous fibers (V) were exposed to radiation under dry conditions at different doses and later analyzed using X-ray diffraction (XRD) and Fourier transform infrared spectroscopy (FTIR). For these measurements, we did not do tomography. The aim was to reach a certain radiation dose in the sample. In a second investigation step, the three inkjet papers were immersed in liquid water to highlight another instance of damage exclusive to this type of paper, which will be described later. The investigation of this wet condition is interesting, as various groups [16-19] show that microcomputed tomography is an excellent method for investigating how liquids interact with fibrous porous media over time.

Micro-computed tomography setup

The pixel size of the two µCT machines are 0.15 and 0.075 mm for the XL and HR, respectively. Both machines use open sources. The performance of an open source can change due to the degradation of the tungsten target. This degradation is constantly monitored with a sharpness test and an intensity signal under the same conditions. Once this degradation exceeds the accepted limits, a new spot on the target is selected by rotating the target.

The dry paper sample P for spectral analysis is attached to an acrylic frame and placed in a 3D-printed holder [20]. This setup maintains the sample in an upright position, perpendicular to the optical axis of the µCT tube, ensuring direct exposure of the paper to the X-rays. The viscous fibers (V) are placed in test tubes. For the liquid-immersed setup (**Fig. 3**), the paper samples are cut into strips and put into a test tube. The filling process involves a syringe pump operated from outside the machine. We used ultrapure water from the Arium Mini device from Sartorius (Göttingen, Germany). The tube in which the samples were placed had a diameter of 1.9 mm, a wall thickness of 0.05 mm, and a length of 100 mm. The test tubes are

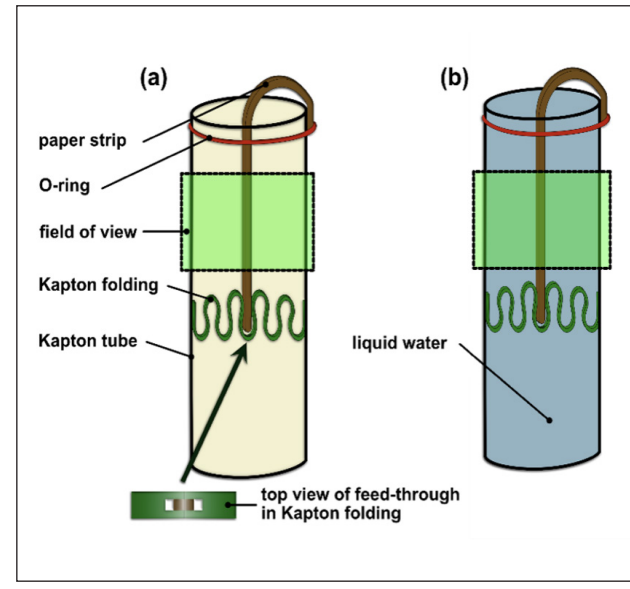

3. Side view of the positioned paper strip in the Kapton tube: (a): An O-ring fixes the paper strip to the upper tube end. The strip is kept in the center of the tube with a piece of Kapton foil folded into a spring-shaped clamp (green). Below image (a) is a top view of the bottom of the tube showing the folded Kapton piece. This piece contains a cutout used as a feed through to supply the paper strip with water from beneath. Highlighted in green is the field of view of which area the µCT scan is taken. Image (b) illustrates the setup, as shown in (a), but filled with water from the syringe pump.

made from Kapton, which was chosen for their excellent X-ray transparency [21].

In our experiments, applying a specific dose at the same position of each sample was sufficient; thus, no rotation was necessary. During the irradiation, no additional filters were placed in front of the tube, and the ventilation inside the µCT machine was turned off to prevent the samples from moving. In all cases, we assume that the calculated dose was applied to the surface of the samples facing the focus of the tube.

X-ray diffraction analysis

The XRD spectra of paper sample P in an irradiated and non-irradiated state were done in an Empyrian (Malvern Panalytical; Malvern, UK) at an acceleration voltage of 40 kV, a current of 40 mA, a range for 2θ from 10° to 42°, and for a duration of 1 h.

From the XRD scans, Segal's crystallinity index [22,23] was calculated:

$$CI = \frac{\left(I_{(002)} - I_{(am)}\right)}{I_{(002)}} \cdot 100 \quad (6)$$

where CI is the calculated crystallinity index [23,24] in %; I_{002} is the intensity (counts in XRD) at $2\theta \sim 22.5°$; and I_{am} is the intensity (counts in XRD) at $2\theta \sim 18.5°$.

Fourier transform infrared spectroscopy

The FTIR analysis was carried out on a Bruker Invenio 3 instrument (Bruker; Villerica, MA, USA). All spectra were recorded in the range of 4000 to 400 cm^{-1}, taking 100 scans at a 4 cm^{-1} resolution. The FTIR was used in attenuated total reflection (ATR) mode with a diamond crystal. The samples were kept for more than 2 h or overnight before scans were taken to reduce peaks of water (H_2O) and carbon dioxide (CO_2) from the laboratory air.

RESULTS AND DISCUSSION

Dose estimations

The air kerma values determined for our X-ray devices can be used in combination with Eq. 1 through Eq. 5 to estimate the dose. We demonstrate this estimation (following Fig. 1) with an example. The water-equivalent absorbed dose, D_{water}, delivered to the cellulose sample contained within a small water-filled tube irradiated under the specified conditions, is approximately 41 kGy, according to **Table I**. The starting point for this estimate

Scan Parameters	
Tube potential/filter	80 kV / no filter
Tube current	88 µA
Scan time	1740 s
Source-object-distance (SOD)	2.7 mm
Diameter of water-filled tube	2 mm
Air Kerma	
From Table A-III K_{air} at SOD = 400 mm	21.2 mGy/mAs
Time current product	153.12 mAs
K_{air} at SOD = 400 mm	3.25 Gy
Inverse square law at SOD = 2.7 mm (Eq. 1) K_{air} at SOD = 2.7 mm	71 kGy
Absorbed Dose	
From Fig. A-1 HVL_1 (80 kV, no filter)	0.1 mm Al
From Fig. A-3 ratio mass energy-absorption water, air calculating dose to water	1.04
D_{water} (without attenuation) (Eq. 2 and Eq. 5)	74 kGy
Attenuation of 1 mm water in front of sample (tube radius) Attenuation factor (calculated with SpekPy [11,12])	0.56
D_{water} (1 mm water) (Eqs. 2, 4, and 5)	41 kGy

I. Estimation of dose. The referenced figures and table are found in the Appendix.

is that the water-filled tube of diameter 2 mm is placed in the radiation field of X-ray tube HR XWT-160-TCNF at a distance of 2.7 mm.

All calculation steps contribute to an increase in the uncertainty on the final estimate of the absorbed dose. A comprehensive estimation of factors influencing the uncertainty is beyond the scope of this work; a more detailed list of such factors is compiled in the Appendix. However, three aspects are worth highlighting:

1. The estimation of the absorbed dose D, based on the measured K_{air}, relies on assumptions about the sample itself. Failing to meet those assumptions considerably increases the uncertainties on the resulting absorbed dose.
2. Ageing of the focal spot on the anode can considerably decrease the output of the X-ray tube. As all measurements were done with a new or almost new focus spot position, the results can be considered as upper limits for aged focal spots.
3. Estimations when using unfiltered beams are challenging, because no standard calibrations (to get N_K factors in this HVL_1 range) are available that cover the required range of beam parameters. Failing to apply chamber correction factors may lead to inaccuracies of up to 20 %.

Using the presented workflow allows estimating the absorbed dose to a reasonably small sample. Depending on the sample size and composition, as well as the energy distribution of the X-ray beam during a rotational scan, the dose throughout an actual sample will not be homogeneous. In most realistic scenarios, the absorbed dose will be highest at the sample surface while showing a gradient across the volume. Detailed information about the dose distribution in a complex, heterogeneous sample can only be provided by a comprehensive Monte Carlo Radiation Transport Simulation. Monte Carlo code systems such as EGSnrc [25] or PENELOPE [26] are used.

Case study on paper-based materials

All further discussed effects are radiation-induced only and cannot be associated with heating the samples. The samples were not rotated while applying the dose. A rotated sample would have different doses on different positions. A representative batch of irradiation tests was done while monitoring the temperature of the sample using an optris PI IR camera with a PI 640i lens (Optris; Berlin). Here, a maximum increase of the sample surface temperature was measured to 4 K.

X-ray diffraction analysis

We verified [24,27] that at low doses (<100 kGy), the crystallinity index of paper P remains relatively unchanged. In the Appendix, **Table A-VII** lists the calculated values for the crystallinity index and **Fig. A-5** shows the XRD results in detail.

Fourier transform infrared spectroscopy analysis of paper

Figure 4P.I shows basically no difference between low-dose and plain paper, indicating no change in vibration modes nor any damage. Above a dose of 50 kGy (Fig. 4 P.II), the irradiated paper shows less pronounced water peaks, and the change in band shapes indicates the absorption of energy, subsequently changing vibration modes of functional groups, but there is no significant radiation damage observed. The assignments of the IR peaks are given in **Table A-VIII** in the Appendix.

Fourier transform infrared spectroscopy analysis of viscous fibers

When examining viscous fibers, significant changes emerge at doses exceeding 64.4 kGy. Line (l1) in Fig. 4-V.I and Fig. 4-V.III shows the O-H band. At this dose, we observe a shift to lower wave numbers, with the peaks gradually becoming narrower and more intense compared to the non-irradiated state [27]. This shift of the O-H band (l1) indicates the destruction of intramolecular hydrogen bonds [22]. The C-H stretching (l2) band is narrower and higher in intensity. The C-H stretching, highlighted by line (l2) on the same graph, exhibits a similar behavior. Both effects correspond to decreasing absorption due to thermal treatment [28] above 300°C. Focusing on Fig. 4-V.II and Fig. 4-V.IV, the shift of peaks continues at 1600 cm^{-1}.

For wavenumbers below 1500 cm^{-1}, alterations can be seen, starting at a dose of 57.6 kGy. The band between 1200 cm^{-1} and 1500 cm^{-1} (ascribed to –C-C and –C-O vibrations, indicating structural changes to the polymer backbone of the cellulose [24]) starts to build a shoulder towards higher wave numbers. The higher transmittance (or lower absorbance) around 1060 cm^{-1} (C-O vibrations) and 1160 cm^{-1} (C-O-C vibrations) indicate the beginning of breakage of the chain structure [28].

By comparing Fig. 4-V.II and Fig. 4-V.IV, we find that the peak at ~ 900 cm^{-1} is no longer present at doses above 212 kGy. The loss of C-O stretching bands at 1600 cm^{-1} (l3), emerging C=O vibrations around 1730 cm^{-1} [24,27], and increase of the three peaks at 1058, 1112, and 1164 cm^{-1} combined with a loss of the peak at ~ 900 cm^{-1} (l4) can be ascribed to a ring rupture [27,28] for 1.47 MGy and beginning ring rupture at 212 kGy. The increase of peaks in the 1237–1370 cm^{-1} region can be ascribed to structural damage of fibers [24,28,29]. In **Fig. A-6** in the Appendix, the raw data can be seen.

Optical analysis

When extracting the high-dose samples (above 200 kGy) from the tube, both fibers showed a discoloring from white to dark yellow/orange, which was more significant at a higher dose. Apart from the discoloring, the structural integrity of the samples was weakened in a way that the 1.47 MGy sample broke at the position of the focal plane.

Closer examination with an optical microscope reveals

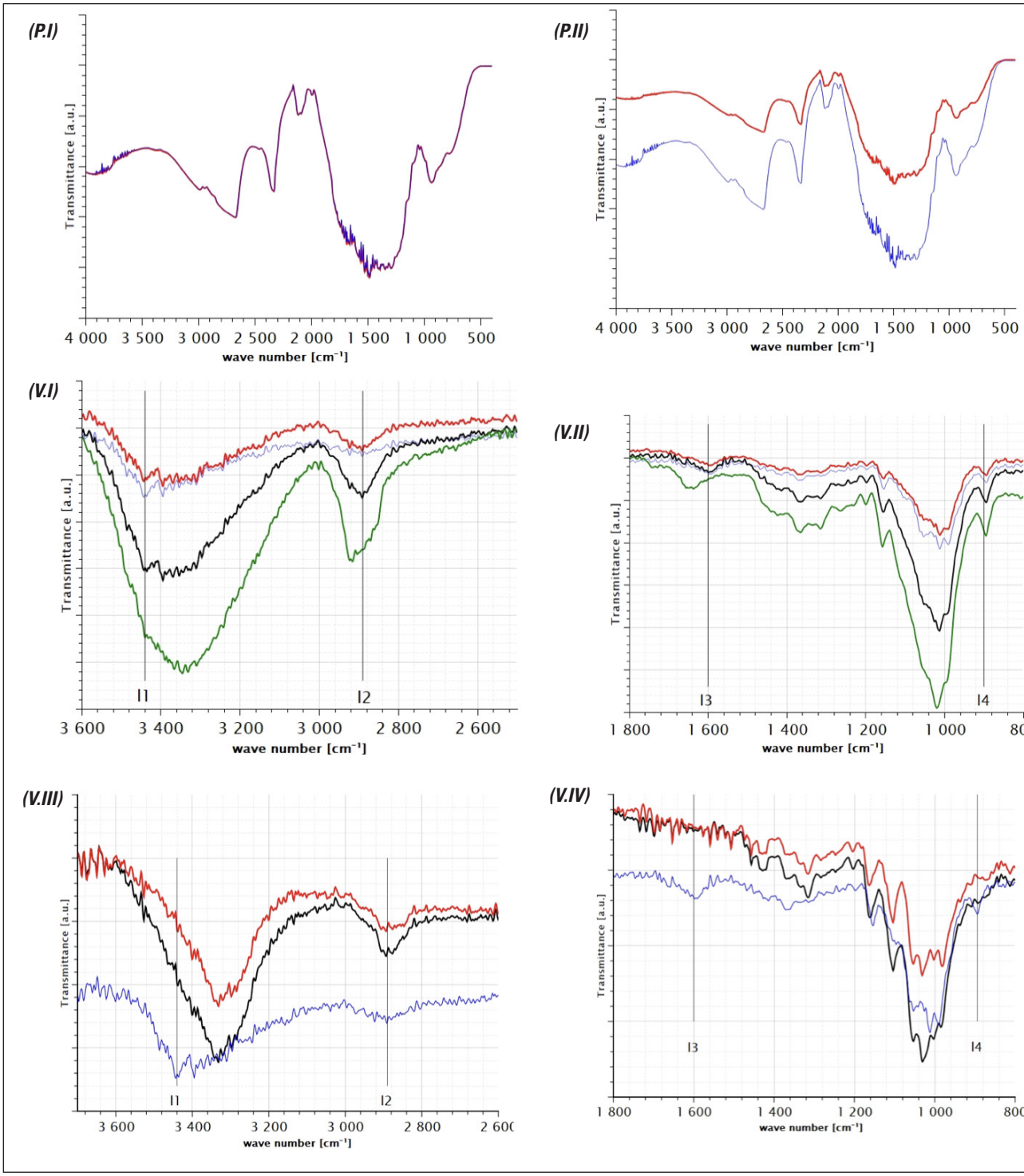

4. Sections P.I and P.II present the single channel spectra for paper P. The blue curve represents the spectrum of non-radiated paper, whereas the red curves illustrate data from radiated samples. At a low dose of 3780 Gy, no significant changes are visible (P.I). However, at a higher dose of 50 kGy, the paper sample exhibits noticeable differences compared to the reference (P.II).

Sections V.I to V.IV present attenuated total reflectance (ATR) spectra of viscous fibers V. The blue curve represents the spectrum of non-radiated fibers, while other colors represent different applied doses. Sections V.I and V.II (lower dose) and V.III and V.IV (higher dose) show different ranges of the same obtained spectra in more detail. Lower doses of 49 kGy (black) and 57.6 kGy (red) do not shift, while at 64.4 kGy (green), shifts can be observed. This trend continues in V.III and V.IV, where the spectra for 212 kGy (black) and 1.47 MGy (red) also show shifted peaks, altered peak shape, and peak loss.

Lines I1 and I2 indicate wave numbers of 3440 cm^{-1} and 2890 cm^{-1}. Lines I3 and I4 indicate wave numbers of 1600 cm^{-1} and 894 cm^{-1}. The region between 1800 and 2300 cm^{-1} can be assigned to the diamond of the ATR crystal.

5. A tampon shaped cellulose sample was irradiated in Unitom HR µCT at a voltage of 40 kV and a current of 100 µA at a SOD of 8.69 mm to sample center (1.69 mm to the sample surface) and for a duration of 16 h and 29 min. The total dose was calculated to 4.35 MGy using Appendix Table A-III.

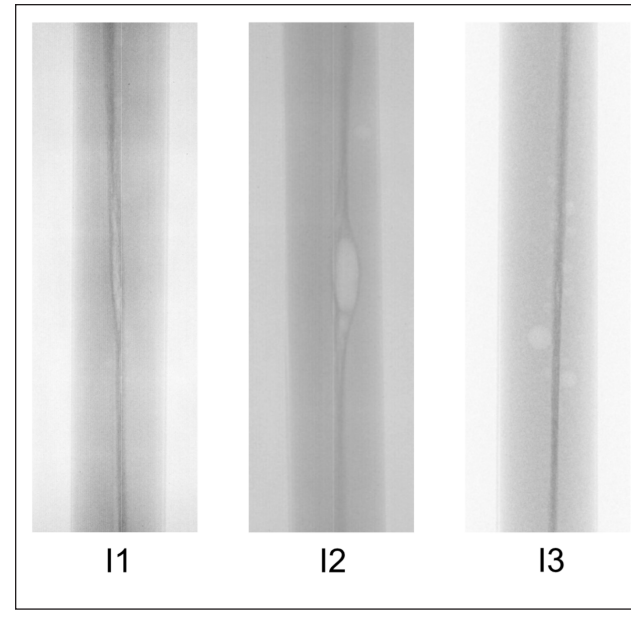

6. The figure compares the three papers — I1, I2, and I3 — after irradiation of 1 h in a fully flooded setup as shown in Fig. 3b. Paper I1 shows a small but elongated delamination, I2 shows a big main bubble, and I3 shows many small bubbles on the surface, although there is only minor delamination inside the paper.

that some fibers seem molten, have a reduced diameter, and no longer maintain a flat shape. Discoloration, observable under magnification, serves as an optical sign of pyrolysis. The corresponding images are presented in the Appendix (**Fig. A-7**).

These effects are visible not only for loose cotton wool but also for compressed viscose fibers in the shape of a tampon, as displayed in **Fig. 5** with the corresponding acquisition settings. After the measurement, we find a bidirectional color gradient, where the maximum discoloration is at the position of the focal plane. The color change becomes more insignificant towards the edges, where the original color remains visible [20].

Paper immersed in liquid water

Another visually observable effect of irradiating paper samples can be seen by immersing inkjet papers in water. A delamination and gas formation can be seen, which differs in detail between different degrees of sizing of otherwise identical papers. In the first test, all three inkjet papers (I1 to I3) were scanned for 1 h at an SOD of 2.67 mm. The previously described effects are shown in **Fig. 6**. The exposure time of 1 h was necessary to get enough contrast between fiber, water, and gas phase.

The influence of the distance between the sample and the source and the resulting delamination effects on the sample are studied. Therefore, a scan series with different SOD is performed. The samples are radiated from one side without rotating the sample stage for 20 min, after which a radiograph is taken. **Figure 7** shows the performed scan series, where the distance was reduced after each 20-min radiation time. With this series, it can be seen that the effects of delamination decrease with increasing SOD, and even at a distance of 5 mm, delamination cannot be detected. In the series, the total exposure time only plays a minor role, as delamination effects can be observed at small SOD distances of < 3 mm in about 10 min, as seen in other scans.

The delamination is irreversible and remains visible even after dry conditions have been reached again. This can be seen from another scan series conducted as follows. The samples are completely immersed in water for 1 h and simultaneously radiated. Before emptying the tube, a radiograph is taken. After 1 h of drying and after 24 h, another radiograph is performed. A schematic of the timeline and the radiographs of these two series are displayed in **Fig. 8**.

Gases were only formed during the irradiation of papers containing calcium carbonate fillers, which were identified as the main contributing factor. As reported by Costagliola et al. [30], the interaction between X-rays and calcium carbonate in water can produce hydrogen. When calcite samples are exposed to a helium ion beam, the radiolysis of water on the surface of the calcite leads to the formation of molecular hydrogen. In biphasic water-calcite systems, the radiolytic production of hydrogen is

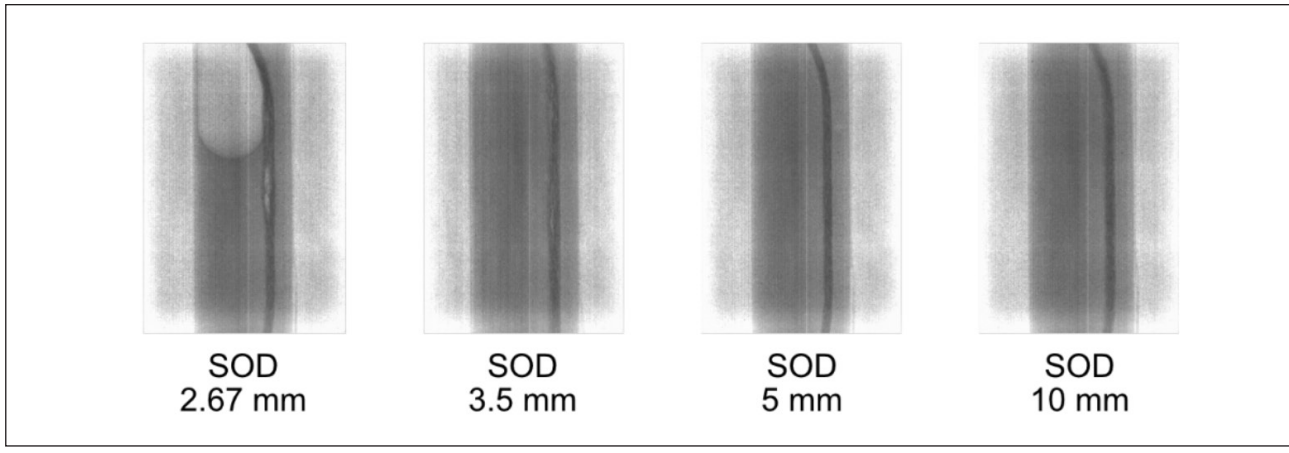

7. Source-object-distance (SOD) measurement series with paper I1. This graphic shows the decreasing influence of radiation over the decreasing distance between the radiation source and the sample (SOD). The sample is irradiated for 20 min in a fully flooded tube, and then moved closer to the source in a stepwise manner.

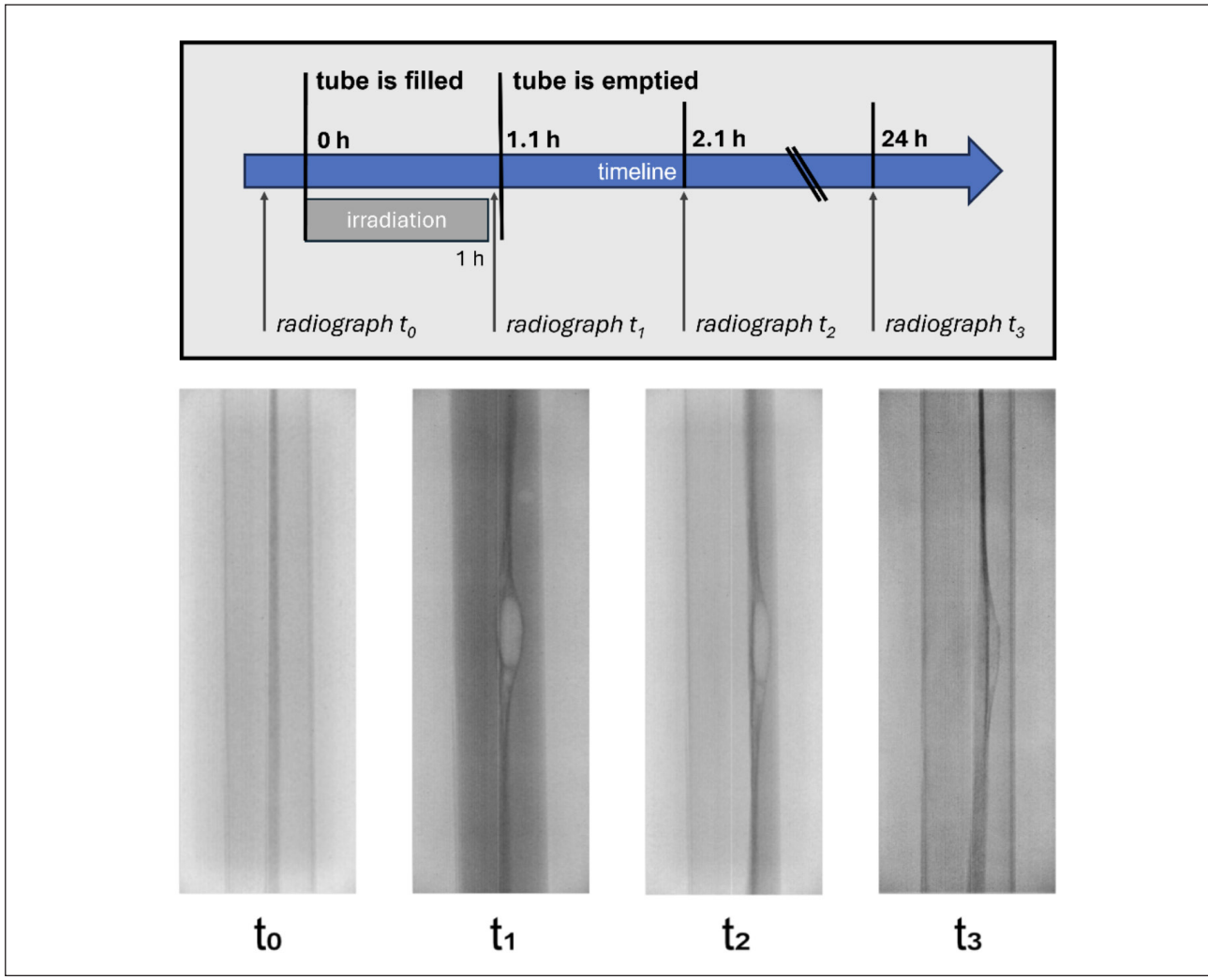

8. Delamination scan series of paper I2 cut in machine-direction (MD): t_0 shows the radiograph in dry state; t_1 shows strip immersed in water and irradiated for 1 h; t_2 shows the strip after 1 h of drying without applying radiation during the drying time; and t_3 shows the strip after 1 day of drying with no applied radiation during the drying period. In MD, the hygroexpansion does not introduce an additional bend in the paper and the sample stays much more stable. In t_3, it becomes clear that the introduced delamination is irreversible, even after drying.

enhanced due to the scavenging effect of carbonate ions. This process reduces the formation of hydroxyl radicals (OH•), which would otherwise recombine with hydrogen. The calcite serves as a source of carbonate ions, supporting continuous hydrogen production, which is unlike in pure water, where hydrogen production stabilizes as the dose increases [30]. As a comparison we also used two different kraft papers (no fillers). We did not find gas formation in this case.

Tests were conducted to confirm the presence of hydrogen. In a larger setup (Appendix **Fig. A-8**), more paper is placed closer to the tube in an attempt to increase gas production. Paper I3 was used for this test, as the gases would stick to its surface, making extraction easier than with the other papers (Appendix **Fig. A-9**). The oxyhydrogen flame test and the hydrogen leak detector test with the detector UCAR Model SP-204SC (RKI Instruments; Union City, CA, USA) gave a positive result, supporting our initial suspicion.

The bubble retention could be due to the inability of the gas to escape from the dense structure of the sample. The papers were extensively investigated using pore network modeling techniques (openPNM). Under dry conditions, no enclosed voids could be identified. All parts of the pore space are connected to the surface. As can be seen in the case of the most hydrophobic paper, the bubbles are also stable on the surface. Therefore, the "rigidity" of the bubbles may be high enough that they do not escape to the surface, even if there is an opening, but instead destroy the paper beforehand.

CONCLUSIONS

Dose measurements

The presented workflow allows estimation of the absorbed dose to a reasonably small sample. The following measures should be considered to minimize the absorbed dose to a sample:

- Increase the SOD.
- Limit the scan time and the tube current.
- The fluence of low-energy photons, which are mostly absorbed and consequently do not contribute much to the imaging process, can be reduced by applying filters.
- The data presented in Appendix Table A-III and Table A-IV, along with consideration of the geometrical dependency on the SOD, can aid in estimating acceptable scan parameters.

Radiation damage on dry cellulosic materials

Pyrolysis is one type of thermal decomposition or chemical degradation of (commonly) organic materials at elevated temperatures, often without access to oxygen. It can be caused by thermal treatment or irradiation with γ-rays or X-rays.

X-ray radiation used in µCT machines to analyze bulk samples will not cause radiation damage to cellulosic materials up to an applied dose of about 50–60 kGy, as found by several groups for microcrystalline cellulose.

Applying a dose of about 200 kGy already causes slight discoloring, breaking of fibers, and destruction of intramolecular hydrogen bonds.

For parameters used to increase contrast and resolution, in particular using small SOD combined with long measurement time, it may be easy to reach 1 MGy, and even beyond, which will cause radiation damage at least on the surface of cellulosic samples such as pyrolysis, melting, ring rupture, and structural damage of fibers.

Paper immersed in liquid water

In this case, it was not expected that one would get hydrogen formation from the filler particles that were used in this particular paper. This means that it is of the utmost importance to take possible radiation damage into account when interpreting µCT data.

Prolonged interaction of cellulose-based materials with X-rays predominantly alters the chemical nature of the fiber surfaces. In the case of high dosage, fibers even break.

Measuring the spatial distribution of mass density in air and the related extension and the position of the fibers will be practically unaffected by the beam damage, since the resolution of laboratory µ-CT machines is in the submicrometer and few-micrometer range. Beam damage can affect or even prevent in situ studies, in particular with water.

In-situ studies aiming at swelling or compression, in particular when done under mechanical load, suffer from the altered chemical nature and the ensuing changes in the fiber-fiber interactions. For materials such as filler-containing paper, the radiation-induced activation of filler-related compounds in water may lead to a decomposition and release of gasses. In either of the cases, µ-CT monitors a process that is different from the one intended.

We have shown that it is necessary to have an estimation of the applied radiation doses in a µCT machine, as radiation damage might occur at the scanning parameters needed for a high-quality measurement. If this is the case, one needs to find the right tradeoff between µCT parameters and possible radiation damage.

ACKNOWLEDGEMENTS

Thanks to Christian Hranitzky of the Dosimetrielabor Seibersdorf, Radiation Protection Dosimetry at Seibersdorf Labor GmbH, for his valuable feedback and for supplying the off-label calibration factors.

Co-authors Zojer, Fuchs, Haberl, Machado Charry, and Stennach gratefully acknowledge financial support from the Christian Doppler Research Association, Federal Ministry for Digital and Economic Affairs, and the National Foundation for Research, Technology, and Development, Austria. Thanks go to Martin Spitzbart for supplying the inkjet paper samples.

LITERATURE CITED

1. Thibault, X. and Bloch, J.-F., *Text. Res. J.* 72(6): 480(2002). https://doi.org/10.1177/004051750207200603.
2. Machado-Charry, E., Neumann, M., Lahti, J., et al., *J. Microsc.* 272(1): 35(2018). https://doi.org/10.1111/jmi.12730.
3. Urstöger, G.J., Kulachenko, A., Schennach, R., et al., *Cellulose* 27(15): 8567(2020). https://doi.org/10.1007/s10570-020-03367-4.
4. Neumann, M., Machado-Charry, E., Baikova, E., et al., *Microsc. Microanal.* 27(6): 1305(2021). https://doi.org/10.1017/s1431927621012563.
5. du Roscoat, S.R., Bloch, J.-F., and Thibault, X., *J. Phys. D: Appl. Phys.* 38(10A): A78(2005). https://doi.org/10.1088/0022-3727/38/10A/015.
6. Chinga-Carrasco, G., Axelsson, M., Eriksen, Ø., et al., *J. Pulp Pap. Sci.* 34(1): 13(2008).
7. Holmstad, R., Goel, A., Ramaswamy, S., et al., *Appita J.* 59(5): 370(2006). https://search.informit.org/doi/10.3316/informit.530871391330541.
8. Neumann, M., Gräfensteiner, P., Machado Charry, E., et al., *Adv. Theory Simul.* 7(8): 2301261(2024). https://doi.org/10.1002/adts.202301261.
9. Seltzer, S.M., Bartlett, D.T., Burns, D.T., et al., *J. ICRU* 11(1): 1(2011). https://doi.org/10.1093/jicru/ndr011.
10. Poludniowski, G., Omar, A., and Andreo, P., *Calculating X-ray Tube Spectra: Analytical and Monte Carlo Approaches*, CRC Press, Boca Raton, FL, USA, 2022.
11. Bujila, R., Omar, A., and Poludniowski, G., *Phys. Med.* 75: 44(2020). https://doi.org/10.1016/j.ejmp.2020.04.026.
12. Poludniowski, G., Omar, A., Bujila, R., et al., *Med. Phys.* 48(7): 3630(2021). https://doi.org/10.1002/mp.14945.
13. *aRTist - Analytical RT Inspection Simulation Tool*, BAM Federal Institute for Materials Research and Testing, Berlin. Available [Online] https://www.artist.bam.de/en/index.htm <03March2026>.

ABOUT THIS PAPER

Cite this article as:
Apfolter, A., Schindler P., Haberl, V., et al., *TAPPI J.* 25(3): 129(2026). https://doi.org/10.32964/TJ25.3.129

DOI: https://doi.org/10.32964/TJ25.3.129

ISSN: 0734-1415

Publisher: TAPPI Press

About this journal

ABOUT THE AUTHORS

Apfolter

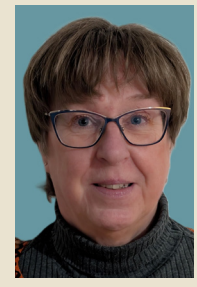

Schindler

Haberl

Fuchs

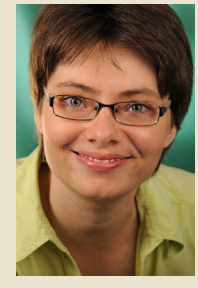

Zojer

Charry

Schennach

We studied this topic because we think micro-computed tomography (µCT) is an important and growing method in paper research. Therefore, radiation damage needs to be taken into account, so we investigated paper properties using µCT.

The most difficult part of this study was obtaining the dose values. We achieved this through cooperation with a medical university.

Through this study, we discovered that radiation damage is something one should keep in mind before the first measurement. It was interesting to find that the doses can be so high, but we did discover that a good analysis of the pore network might be problematic due to radiation damage in the analysis.

Our next steps are aimed at getting better insight into this radiation damage.

Apfolter works in X-ray maintenance in the Department of Radiation Oncology, LKH University Hospital, Graz, Austria. Schindler is a Master's student in the Institute of Software Engineering and Artificial Intelligence and the Institute of Solid-State Physics at Graz University of Technology, Graz, Austria. Haberl and Fuchs are Master's students in the CD-Laboratory for Mass Transport through Paper at Graz University of Technology, Graz, Austria. Zojer is professor; Charry is senior scientist; and Schennach is professor in the CD-Laboratory for Mass Transport through Paper and the Institute of Solid-State Physics at Graz University of Technology, Graz, Austria. Email Schennach at robert.schennach@tugraz.at.

14. Araki, F., *Radiat. Phys. Chem.* 188: 109595(2021), https://doi.org/10.1016/j.radphyschem.2021.109595.
15. *XCOM: Photon Cross Sections Database*, National Institute of Standards and Technology, Physical Measurement Laboratory, Gaithersburg, MD, USA. Available [Online] https://physics.nist.gov/PhysRefData/Xcom/html/xcom1.html <03March2026>.
16. Fuchs, M., Machado Charry, E., Böhm, G., et al., "Where is the water," in *Advances in Pulp and Paper Research, Cambridge 2022, Trans. of the XVIIth Fund. Res. Symp. Cambridge, 2022* (D. Coffin and W. Batchelor, Eds.), FRC, Manchester, 2022, pp. 495–510. https://doi.org/10.15376/frc.2022.1.495.
17. Ferreira, E.S., Drummond, J., Veiga, A.T.V., et al., *Carbohydr. Polym.* 311: 120785(2023). https://doi.org/10.1016/j.carbpol.2023.120785.
18. Wegele, P., Rosén, T., and Söderberg, D., *Exp. Fluids* 65(9): 140(2024). https://doi.org/10.1007/s00348-024-03869-y.
19. Fischer, R., Schlepütz, C.M., Hegemann, D., et al., *Phys. Rev. E* 103(5): 053101(2021). https://doi.org/10.1103/PhysRevE.103.053101.
20. Schindler, P., "Impact of µCT measurement parameters on applied dose and radiation damage on cellulosic materials," Master's thesis, Graz University of Technology (TU Graz), Graz, Austria, 2025.
21. Megusar, J., *J. Nucl. Mater.* 245(2): 185(1997). https://doi.org/10.1016/S0022-3115(97)00012-3.
22. Sun, J., Xu, L., and Ge, M., *J. Appl. Polym. Sci.* 127(3): 1630(2013). https://doi.org/10.1002/APP.37544.
23. Yang, G., Zhang, Y., and Wei, M., *Carbohydr. Polym.* 81: 114(2010), https://doi.org/10.1016/j.carbpol.2010.02.003.
24. List, R., Gonzalez-Lopez, L., and Ashfaq, A., *Polymers* 15(23): 4483(2023). https://doi.org/10.3390/polym15234483.
25. Kawrakow, I., Rogers, D.W.O., Mainegra-Hing, E., et al., *EGSnrc Toolkit for Monte Carlo Simulation of Ionizing Radiation Transport*, National Research Council Canada, Metrology Research Centre, Ottawa, 2000. https://doi.org/10.4224/40001303.
26. *PENELOPE: A Code System for Monte Carlo Simulation of Electron and Photon Transport*, Organisation for Economic Co-operation and Development (OECD), Paris, 2019. https://doi.org/10.1787/32da5043-en.
27. Andreev, M., Marmiroli, B., and Schennach, R., *Microelectron. Eng.* 256: 111720(2022). https://doi.org/10.1016/j.mee.2022.111720.
28. Parihar, A., Vongsvivut, J., and Bhattacharya, *ACS Omega* 4: 8747(2019). https://doi.org/10.1021/acsomega.8b03681.
29. Su, X.-J., Zhang, C.-Y., and Li, W.-J., *Appl. Sci.* 10(3): 1130(2020). https://doi.org/10.3390/app10031130.
30. Costagliola, A., Vandenborre, J., Blain, G., et al., *J. Phys. Chem.* C 121(44): 24548(2017). https://doi.org/10.1021/acs.jpcc.7b07299.
31. Andreo, P., Burns, D.T., Nahum, A.E., et al., *Fundamentals of Ionizing Radiation Dosimetry*, Wiley-VCH, Weinheim, Germany, 2017.
32. Seltzer, S.M., Fernandez-Varea, J.M., Andreo, P., et al., *Key Data for Ionizing-Radiation Dosimetry: Measurement Standards and Applications*, ICRU Report 90, International Commission on Radiation Units and Measurements, Bethesda, MD, USA, 2016.
33. Andreo, P., *Phys. Med. Biol.* 64(20): 205019(2019), https://doi.org/10.1088/1361-6560/ab421d.
34. *X-Ray Mass Attenuation Coefficients*, National Institute of Standards and Technology, Gaithersburg, MD, USA. Available [Online] https://www.nist.gov/pml/x-ray-mass-attenuation-coefficients <05March2026>.

APPENDIX

A1. Rationale for inferring the dose D_{med} from the kerma K_{air} in free air

An accessible text about this subject is available in [10]. Comprehensive information about radiation dosimetry in general is given by Andreo et. al [31].

For a given photon energy E and the fluence in a medium Φ_{med}, i.e., the radiant energy per unit time and per photon energy emitted into the medium, the kerma K_{med} can be calculated as follows for each photon energy:

$$K_{\text{med}} = E \times \Phi_{med} \times \left[\frac{\mu_{tr}(E)}{\rho}\right]_{med}$$

where $\left[\frac{\mu_{tr}(E)}{\rho}\right]_{med}$ is the mass energy-transfer coefficient of a given medium.

In the energy range E <300 KeV, almost all transferred energy is deposited locally in the medium, while other loss mechanisms such as Bremsstrahlung are negligible. Therefore, the mass energy-transfer coefficient $\left[\frac{\mu_{tr}(E)}{\rho}\right]_{med}$ is practically equal to mass energy-absorption coefficient $\left[\frac{\mu_{en}(E)}{\rho}\right]_{med}$ that describes the local absorption of energy [10].

In situations involving additional charged particle equilibrium, it can be concluded that the absorbed dose D is numerically the same as the kerma K:

$$D_{\text{med}} \approx K_{med} \approx E \times \Phi_{med} \times \left[\frac{\mu_{en}(E)}{\rho}\right]_{med}$$

Given a small enough sample of a medium embedded in air, where the disturbance of the fluence is negligible, the

dose to the medium is directly proportional to the ratio of the mass energy-absorption coefficients of the medium and air. With a known air kerma in air, K_{air}, the absorbed dose to medium is given by:

$$D_{med} \approx K_{med} \approx K_{air} \times \frac{\left[\frac{\mu_{en}(E)}{\rho}\right]_{med}}{\left[\frac{\mu_{en}(E)}{\rho}\right]_{air}} \quad .$$

This equation is only valid for monoenergetic photons of energy E. In case of a photon beam with a photon fluence spectrum Φ_{med}, the mass energy-absorption coefficients must be integrated over the range of photon energies:

$$D_{med} \approx K_{air} \times \frac{\int_0^{Emax} E \times \Phi_E \times \left[\frac{\mu_{en}(E)}{\rho}\right]_{med} dE}{\int_0^{Emax} E \times \Phi_E \times \left[\frac{\mu_{en}(E)}{\rho}\right]_{air} dE} \quad .$$

Sources for finding the mass energy-absorption coefficients for a wide range of materials and energies are given in Section A.3 of this Appendix.

A2. Characteristics of the tubes in the two X-ray devices and their associated air kerma calibration factors

This section provides information on the X-ray tubes used (**Table A-I**); the normalized fluence spectra for tube 1, XWT-160-TCNF (**Fig. A-2**); and air kerma free-in-air calibration factors for the ionization chambers (**Table A-II, Fig. A-2**).

	Tube 1	Tube 2
Device	Tescan Unitom HR	Tescan Unitom XL
Manufacturer	X-RAY WorX	X-RAY WorX
Product type	XWT-160-TCNF	XWT-190-CT
Target type	Transmission	Reflection
Tube potential range	20 kV to 160 kV	20 kV to 180 kV
Target	2 µm W	2.0 mm W
Target angle	—	17°
Inherent filtration	300 µm CVD	1.0 mm Be
Additional filtration	0.5 mm Al	1.0 mm Al
	1.0 mm Al	1.5 mm Al
	0.5 mm Cu	1.0 mm Cu
	1.0 mm Cu	1.5 mm Cu
	0.75 mm Sn	0.75 mm Sn
	1.00 mm Sn	1.00 mm Sn

CVD: chemical vapor deposition; Al: aluminum; Cu: copper; Sn: tin; Be: beryllium.

A-I. Technical specifications of the two X-Ray tubes being examined. Transmission source is used in the Tescan Unitom HR, and the reflection source is used in the Tescan Unitom XL.

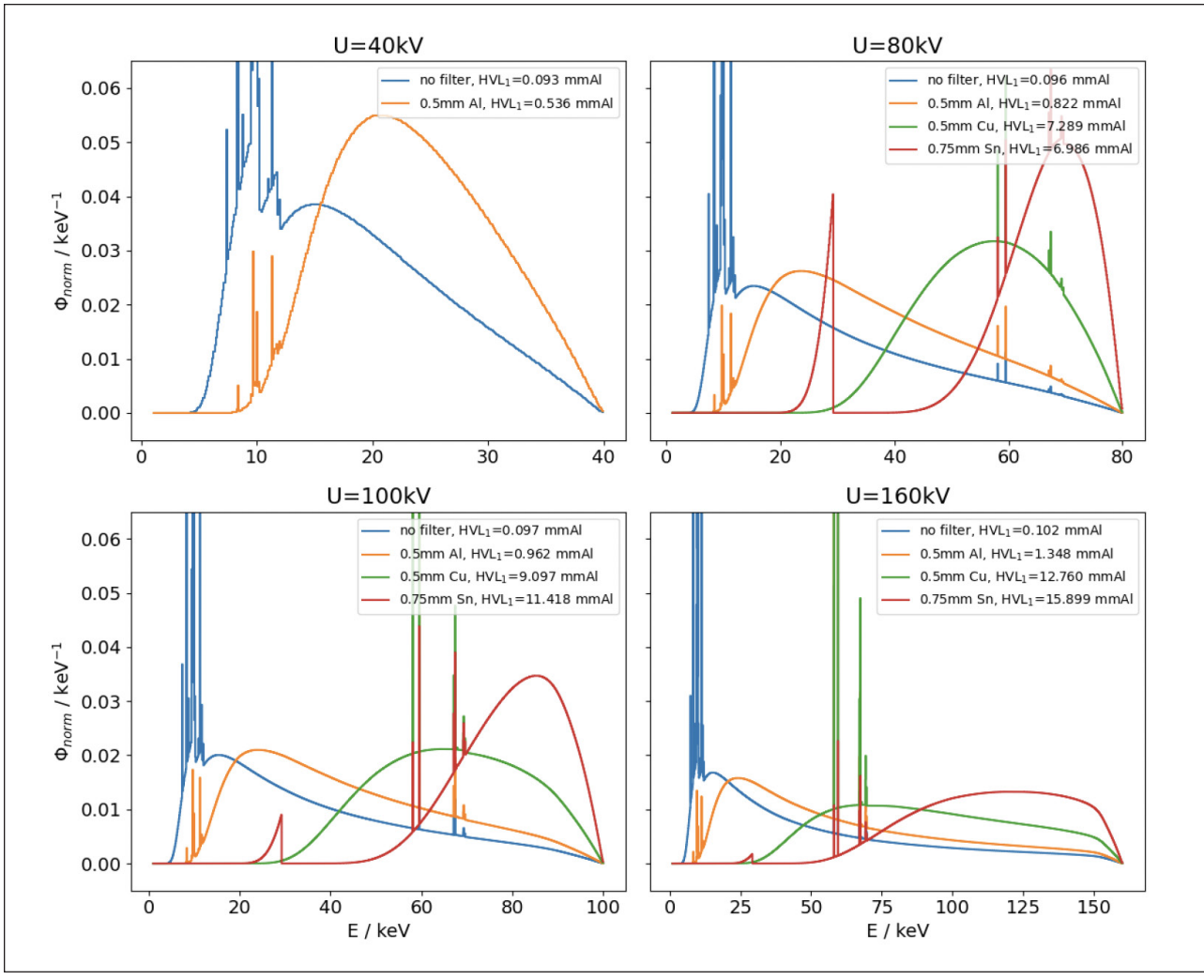

A-1. Selected normalized fluence spectra Φ_{norm} for tube 1 (XWT-160-TCNF) at 400 mm distance to the source. A selection of different combinations of tube potentials U and additional filters is shown. The width of the energy bins ΔE is set to 0.1 keV. The additional filter and the calculated HVL_1 are given in the plots. For better clarity, the fluence axis and therefore the height of the characteristic lines is limited. All calculations are done with SpekPy [11, 12] and aRTist [13].

				PTW 23342	PTW 30013
Spectrum	***U*, kV**	**E_{mean}, keV**	**HVL_1, mm Al**	N_K	N_K
TW30	30	14.6	0.11	0.89*	1.10*
TW50	50	28.4	0.95	0.91*	0.92*
SH50	50	33.9	2.21	0.90*	0.889
TH70	70	41.3	3.01	0.89*	0.887
TH100	100	50.5	3.98	0.87*	0.887
TH135	135	67.4	8.62	0.82*	0.889
TH180	180	84.5	12.08	---	0.890
* Indicates off-label calibration.					

A-II. Air kerma free-in-air calibration factors N_K for the ionization chambers PTW 23342 and PTW 30013. The calibration factors N_K together with the name, the mean photon energy E_{mean}, and HVL_1 for the calibration spectrum are given.

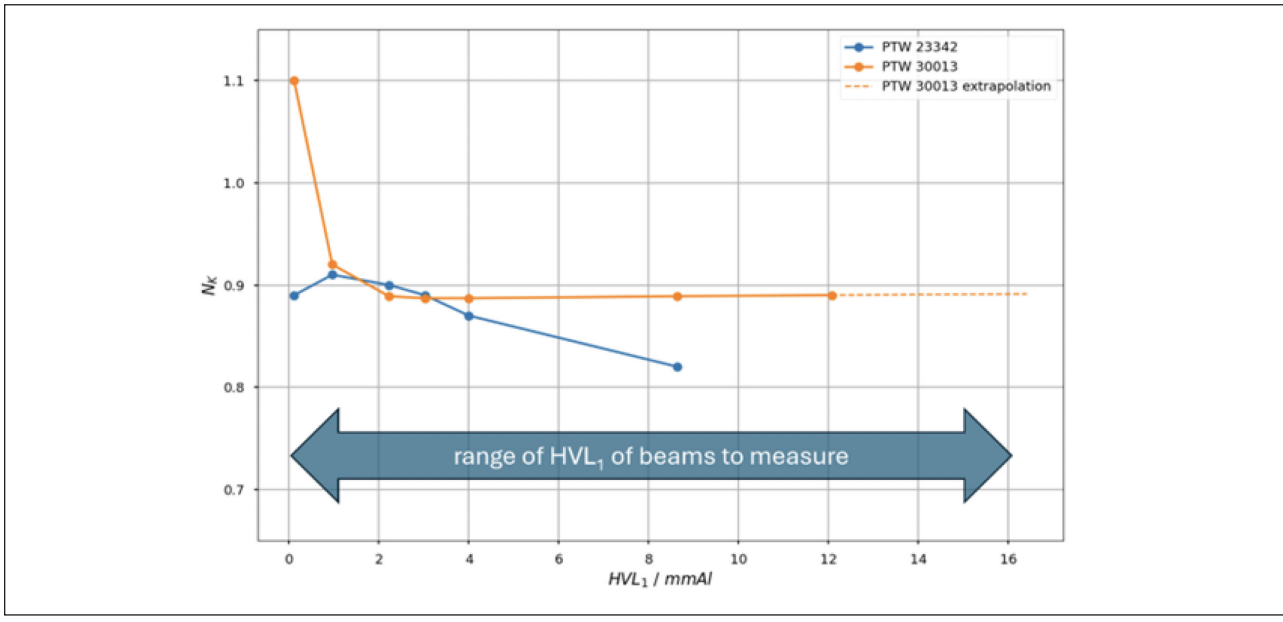

A-2. Calibration factors N_K for air kerma free-in-air for PTW 23342 (blue) and PTW 30013 (orange). The circles are the calibration factors provided by a dosimetry calibration laboratory and include regular and off-label calibrations. For HVL_1 > 2 mm aluminum (Al), the PTW 30013 calibration factor stays almost constant at 0.89. The dashed line indicates an extrapolation over the HVL_1 range needed to correct the air kerma measurements. Due to absorption in the chamber wall, the calibration factor for PTW 30013 shows a steep increase for HVL_1 < 2 mm Al. In contrast, the calibration factor of PTW 23342 shows only weak variations for HVL_1 up to 3 mm Al and decreases gradually to 0.82 for the last HVL_1 value given. The arrow indicates the range of HVL_1 needed for interpolation to get all correction factors.

A3. Data sources for mass energy-absorption coefficients

Data for mass energy-absorption coefficients in air, water, and other materials can be found in [32,33] and from NIST [34]. Ratios of mass energy-absorption coefficients of water-to-air, free-in-air (FIA) as a function of HVL_1 are given in [33] and are reproduced in **Fig. A-3**.

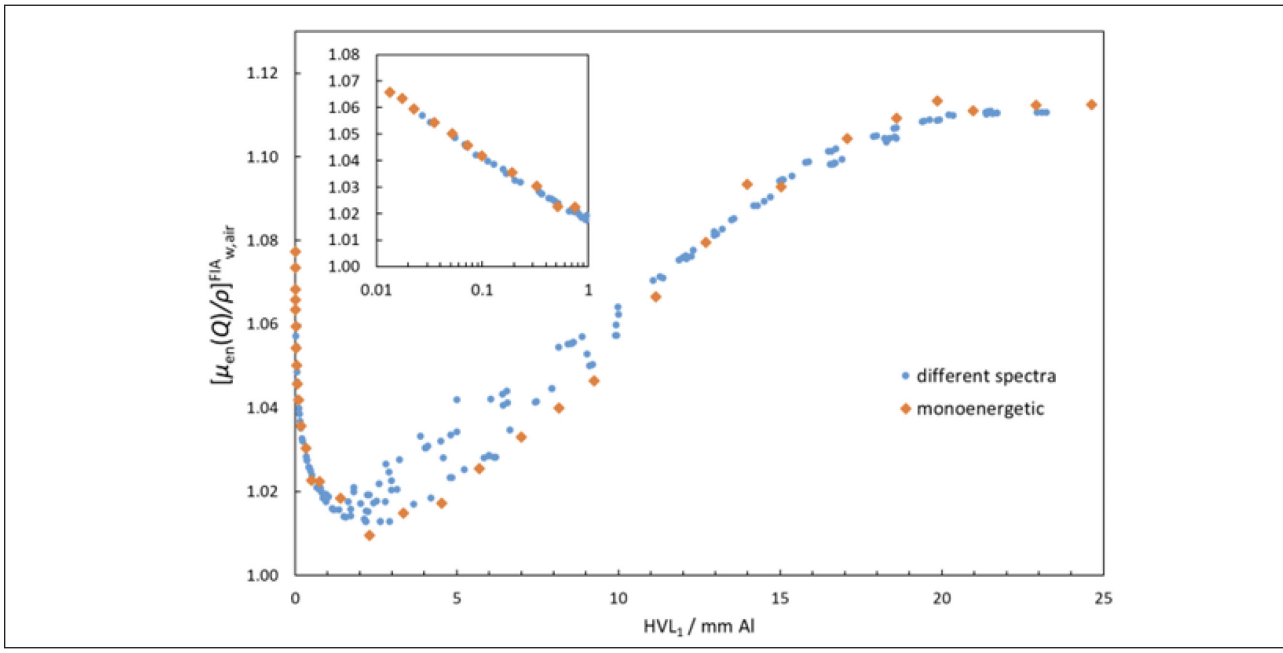

A-3. Ratio of mass energy-absorption coefficients of water to air, free-in-air (FIA) as a function beam quality Q given as HVL_1 for monoenergetic photon beams (orange diamonds) and a wide range of realistic X-ray beam spectra with various combinations of tube potentials and applied filters (blue dots). For clarity, the part for small HVL_1 is inserted with logarithmic scale. Data reproduced from Andreo [33].

A4. Air kerma free-in-air K_{air} values for a variety of operation modes and filters of the two X-ray devices

Table A-III and **Table A-IV** give the parameters necessary to calculate the dose at the sample.

Normalized K_{air}, mGy/mAs							
Source	**+**	**+**	**+**	*****	*****	**#**	**#**
***U*, kV**	**No filter**	**0.5 mm Al**	**1.0 mm Al**	**0.5 mm Cu**	**1.0 mm Cu**	**0.75 mm Sn**	**1.0 mm Sn**
30	7.52E+00	5.57E-01	2.31E-01	4.54E-05	1.00E-07	1.7E-04	2.7E-05
40	1.31E+01	1.16E+00	5.51E-01	2.10E-03	8.01E-05	6.9E-04	1.2E-04
50	1.80E+01	1.72E+00	8.81E-01	1.26E-02	1.49E-03	1.1E-03	2.1E-04
60	2.07E+01	2.12E+00	1.13E+00	3.60E-02	7.56E-03	1.8E-03	3.2E-04
70	2.14E+01	2.34E+00	1.29E+00	7.09E-02	2.12E-02	3.3E-03	8.1E-04
80	2.12E+01	2.46E+00	1.38E+00	1.11E-01	4.25E-02	7.6E-03	2.7E-03
90	2.06E+01	2.55E+00	1.43E+00	1.53E-01	6.93E-02	1.6E-02	7.3E-03
100	2.02E+01	2.63E+00	1.50E+00	1.92E-01	9.89E-02	2.9E-02	1.6E-02
110	1.99E+01	2.70E+00	1.56E+00	2.29E-01	1.29E-01	4.6E-02	2.8E-02
120	1.97E+01	2.81E+00	1.62E+00	2.59E-01	1.63E-01	6.7E-02	4.4E-02
130	1.97E+01	2.94E+00	1.70E+00	3.19E-01	1.97E-01	9.0E-02	6.3E-02
140	1.99E+01	3.07E+00	1.78E+00	3.72E-01	2.32E-01	1.1E-01	8.4E-02
150	2.03E+01	3.22E+00	1.88E+00	4.36E-01	2.63E-01	1.4E-01	1.1E-01
160	2.03E+01	3.45E+00	1.97E+00	5.09E-01	2.89E-01	1.7E-01	1.3E-01

+ Measured with PTW 23342.
* Measured with PTW 30013.
# Calculated with aRTist/SpekPy; no measurements were taken.
Al: aluminum; Cu: copper; Sn: tin.

A-III. Air kerma free-in-air K_{air} normalized to a current-time product of 1 mAs as a function of tube potential U and applied filter for tube 1 (HR XWT 160 TCNF) at SOD = 400 mm. To get the air kerma for an actual scan, the air kerma per current-time product must be multiplied by the tube current and the scan time.

Normalized K_{air}, mGy/mAs							
Source	**+**	**+**	*****	*****	*****	*****	*****
***U*, kV**	**No filter**	**1.0 mm Al**	**1.5 mm Al**	**1.0 mm Cu**	**1.5 mm Cu**	**0.75 mm Sn**	**1.0 mm Sn**
20	3.69E+00						
30	8.13E+00	2.40E-01					
40	1.20E+01	4.79E-01	2.77E-01				
50	1.52E+01	7.12E-01	4.48E-01				
60	1.79E+01	9.50E-01	6.28E-01				
70	2.00E+01	1.19E+00	8.04E-01				
80	2.18E+01	1.43E+00	1.00E+00				
90	2.33E+01	1.66E+00	1.19E+00				
100	2.46E+01	1.93E+00	1.42E+00	1.12E-01	6.28E-02		
110	2.56E+01	2.18E+00	1.64E+00	1.63E-01	9.72E-02		
120	2.65E+01	2.45E+00	1.87E+00	2.24E-01	1.40E-01		
130	2.71E+01	2.71E+00	2.10E+00	2.93E-01	1.92E-01		
140	2.77E+01	2.98E+00	2.34E+00	3.74E-01	2.53E-01		
150	2.83E+01	3.26E+00	2.57E+00	4.65E-01	3.23E-01	2.27E-01	1.60E-01
160	2.88E+01	3.51E+00	2.80E+00	5.64E-01	4.02E-01	2.92E-01	2.12E-01
170				6.74E-01	4.91E-01	3.67E-01	2.74E-01
180				7.95E-01	5.88E-01	4.50E-01	3.44E-01

+ Measured with PTW 23342.
* Measured with PTW 30013.
Al: aluminum; Cu: copper; Sn: tin.

A-IV. Air kerma free-in-air K_{air} normalized to a current-time product of 1 mAs as a function of tube potential U and applied filter for tube 2 (XL XWT 190 CT) at SOD = 400 mm. To get the air kerma for an actual scan, the air kerma per current-time product must be multiplied by the tube current and the scan time.

A5. Comments on uncertainties associated with dose estimates

A comprehensive uncertainty analysis of the estimated absorbed dose is beyond the scope of this work, but remarks are given here:

- The uncertainties (k = 1) of K_{air} in the Table A-III and Table A-IV are estimated to be:
  - 5% for all measurement-based results.
  - 20% in cases where no measurements were taken, and the results are solely based on calculations.
- The uncertainties associated with the absorbed doses, estimated as outlined previously and derived from K_{air}, rely on the specific configuration and therefore cannot generally be specified.
  - The smaller the sample, the lower the uncertainties.
  - The higher the tube potential and the filtration and therefore higher HVL_1, the lower the uncertainties.
  - The inverse square law does not consider the effect of scattered radiation that comes from the air, nearby structures, and the sample itself. Consequently, the uncertainties are rising as SOD decreases.
  - For reasonably small samples, the procedure will give at least the right order of magnitude of the absorbed dose.

A6. Materials and setup

	Dry Sheet Thickness, µm	Base Weight, g/m²	Contact Angle Water @ 0.5s	Porosity (Bendtsen), mL/min	Filler Content PCC, %
P	150	100	122	-	0
I1	110	90	35	890	21.6
I2	110	81	81	1000	21.4
I3	110	109	109	1000	21.4

A-V. List of papers used. The label "Bendtsen porosity" or also "air porosity" refers to the outcome of the standardized Bendtsen measurement, ISO 8791-2:2013 "Paper and board — Determination of roughness/smoothness (air leak methods) — Part 2: Bendtsen method" (PCC: precipitated calcium carbonate).

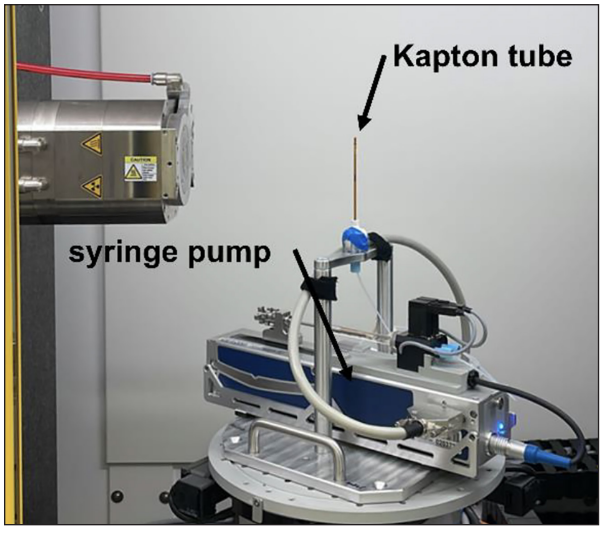

A-4. The photo shows the in-situ setup for micro-computed tomography (µCT) measurement used to create the flooded environment for the paper. The setup can be operated from outside the machine. It consists of the syringe pump with the mounted Kapton tube. Test tubes made from Kapton were chosen for their excellent X-ray transparency [21]. The paper samples are cut into strips and put into a test tube. The tube has a diameter of 1.9 mm, a wall thickness of 0.05 mm, and a length of 100 mm. The paper strips are cut to a size of 1.6 mm x 80 mm. A VLS2.30DT laser cutter from Universal Laser Systems (Scottsdale, AZ, USA) was used to prepare the samples. The cut parameters giving the cleanest cut, with least burning of the paper, was found in an iterative procedure and surveyed using optical microcopy.

A7. X-ray diffraction measurements of radiated and non-radiated samples

The arrows in **Fig. A-5** indicate the regions of the values for 2θ at which the counts (intensities) for the calculation (Eq. 1) of the crystallinity index were taken. Three scans were chosen to illustrate that the band between 2θ = 12°–17° and the peaks at 2θ ~ 22° do not differ significantly in position and shape, and there is no indication of radiation damage or of change in crystallinity.

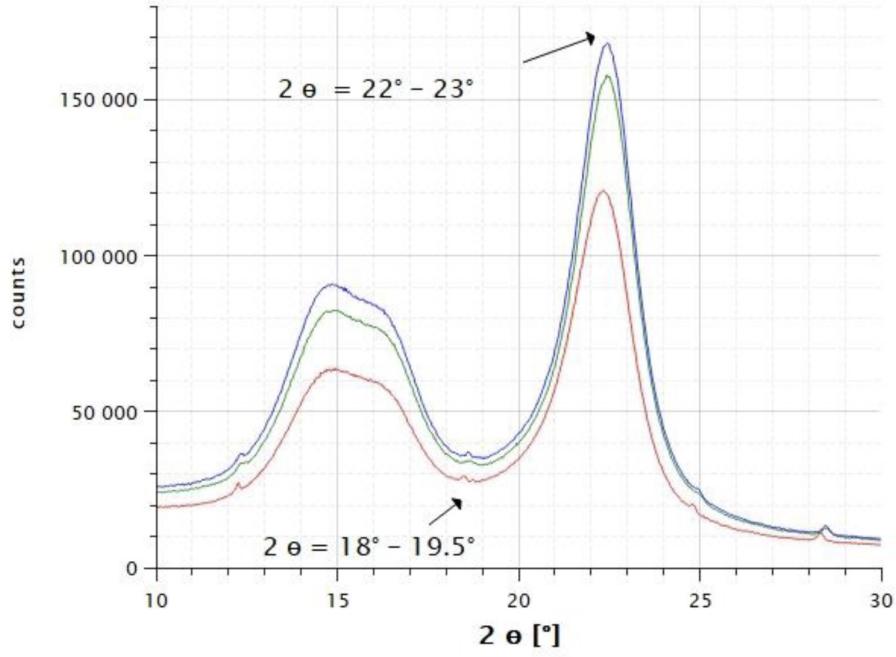

A-5. X-ray diffraction (XRD) scans of paper samples after irradiation with different doses: blue: 0 Gy; red: 3780 Gy; and green 50 kGy.

Sample	*P*, W	*I*, µA	*SOD*, mm	*t*, min	*U*, kV	Dose, Gy
P1	15	188	200	60	80	59
P2	15	188	25	60	80	3,780
P3	150	938	25	120	160	49,000
V1	150	938	25	120	160	49,000
V2	150	1154	25	120	130	57,600
V3	150	1364	25	120	110	64,400
V4	15	375	7	240	40	212,000
V5	150	1154	7	240	130	1,470,000
P: power; *I*: target current; *SOD*: source-to-object distance; *t*: time; *U*: tube potential.						

A-VI. List of the set parameters for paper (P) and viscous fibers (V) samples as well as the respective calculated applied dose.

Sample No.	Applied Dose, Gy (calculated)	CI, %
P1	0	77.43
P2	60	77.64
P3	236	76.70
P4	944	75.80
P5	3780	77.15
P6	15	76.63
P7	50000	78.51

A-VII. Confidence interval (CI) calculated using Eq. 1.

A.8 Fourier transform infrared spectroscopy analysis

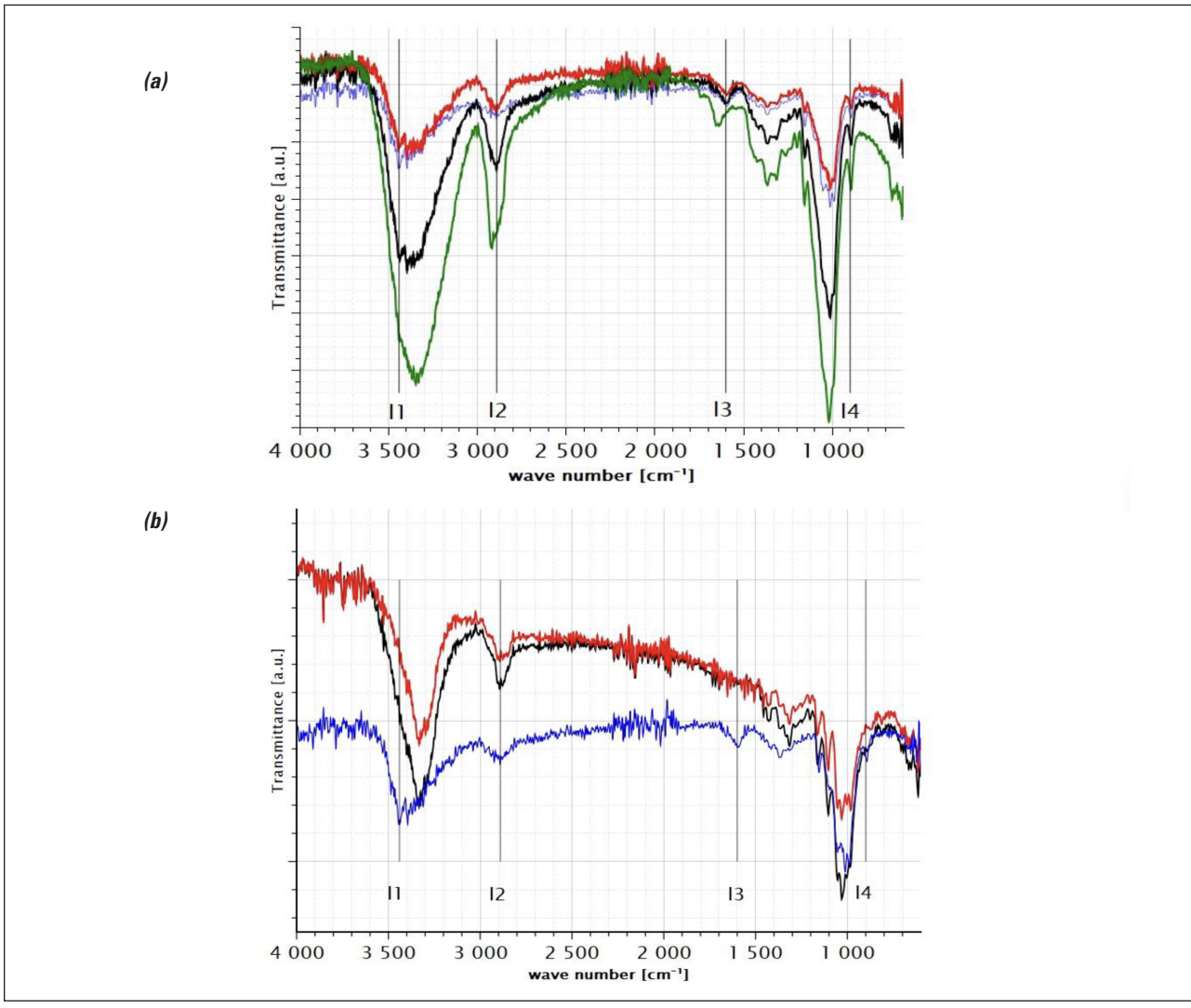

A-6. (a) Spectra of samples V1 (black), V2 (red), V3 (green), and V0 (blue) in the range of wave numbers 600–4000 cm^{-1}. Lines (I1-I4) indicate wave numbers of 3440, 2890, 1600, and 894 cm^{-1} aligned to peaks or bands in the blue spectrum of V0, no reference to background. (b) Spectra of samples V4 (black), V5 (red), and V0 (blue) in the range of wave numbers 600–4000 cm^{-1}. Lines (I1–I4) indicate wave numbers of 3440, 2890, 1600, and 894 cm^{-1} aligned to peaks or bands in the blue spectrum of V0, no reference to background.

Wave Numbers, cm^{-1}	Assignment
3500–3200	OH stretching
~ 2900	CH stretching
2400–2300	CO2
1640	Absorbed H2O
1610–1590	Aromatic skeletal vibrations + C=O
1430	CH
1370	OH
1340–1330	CH2 wagging
1160–1140	C-O-C
1110	Glucose ring stretching, ring vibrations
~ 900	Ring vibrations

A-VIII. Assignment of most prominent vibration modes to wave numbers.

A.9 Optical analysis

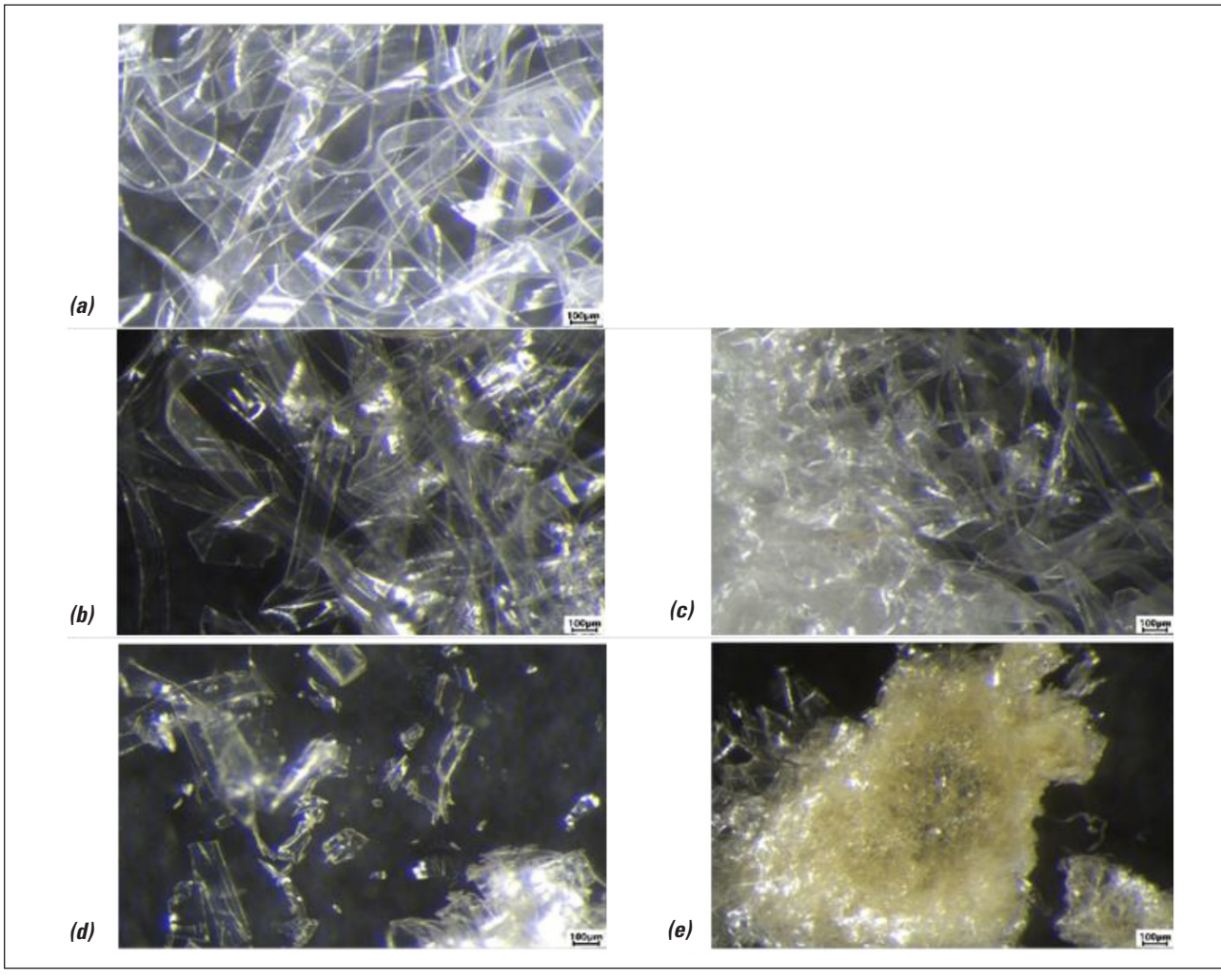

A-7. Images of viscous fibers (V): (a) fibers of V0; (b) V4 showing a few broken fibers; (c): yellowish discoloring; (d) V5 showing many broken fibers; and (e) orange discoloring.

A.10 Gas detection

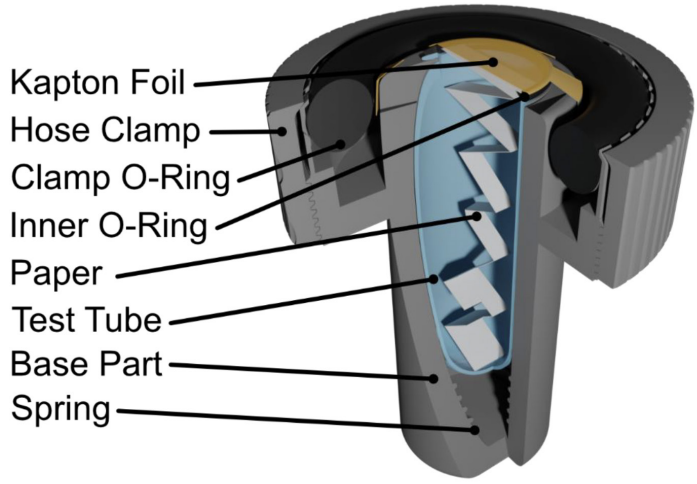

A-8. Gas detection setup consisting of two 3D-printed main parts — the hose clamp and the base part — that are screwed together. Inside the base part, a test tube filled with water contains a folded paper strip. The test tube is closed with a Kapton foil, with a small O-ring between them. The screw connection creates a force on the big O-ring, which presses against the Kapton folding and holds it in place. The spring on the bottom of the base part pushes the test tube firmly against the foil, creating a tight seal for the measurement.

A-9. Photograph showing the gas production under the Kapton foil in the gas detection setup, illustrated in Fig. A-9 with paper I3 after 2 h of irradiation. The first alterations are visible after about 1 to 2 min in radiographs of the scan.